DOE/NV/03624--0361

Approved for public release; distribution is unlimited

Portable COTS RGB Wavefront System for Real-time Turbulence Mitigation

27 February 2019

Ms. Mary O'Neill[1]
Dr. David Terry[2]
Mr. Ian McKenna[1]

[1]Nevada National Security Site (NNSS)/Special Technologies Laboratory (STL)
Santa Barbara, CA 93111, USA
[2]Fifth Gait Technologies, Santa Barbara, CA 93111, USA

ABSTRACT

Atmospheric effects reduce the ability to detect or identify objects of interest due to spatial and spectral scintillation. Algorithms alone cannot correct for turbulence over long-range horizontal paths. While adaptive optics methods work well for astronomical viewing, they are not readily adapted for complex imagery over long-range horizontal paths. At MSS Parallel in 2016, we presented our work for the red/green/blue (RGB) wavefront sensor. Since then, we have completed our system to combine an off-the-shelf high-frame-rate USB3 color camera with a compact 90 mm Maksutov-Cassegrain telescope and an OKO deformable mirror (DM) to create a portable, real-time RGB wavefront sensor and turbulence mitigation system. The telescope's aperture is covered with an aluminum plate holding three separate narrowband color filters. These filters, specifically matched to the relative spectral response of the sensor's Bayer mask, provide nearly complete separation of the three color images. This device enables portable imaging through atmospheric turbulence and analysis thereof, where relative motion of the three-color Bayer-pixel video provides real-time wavefront information on the second-order statistics of Kolmogorov turbulence. We measured relative RGB pixel shifts and controlled this mirror using an ODROID single-board computer. We developed a bench setup to calibrate the relationship between pixel shifts and the deformable mirror actuators. We demonstrated the feasibility of this system on a benchtop and on scenes at 700 meters showing real time correction.

Keywords: Adaptive Optics, Shack-Hartmann sensor, remote sensing, wavefront sensing, turbulence

1.0 Background

There are three major effects of the atmosphere on a propagating wave: absorption, scattering, and refractive-index fluctuations (optical turbulence). Atmospheric turbulence–induced image degradation presents a significant problem in extended range surveillance and signal processing because, in many applications, these effects are more restrictive to viewing resolution than the diffraction limit.

Turbulence is strongest when there is a large temperature differential between the earth (ground) and the surrounding air. When the earth is warmed by the sun, energy is injected back into the air as wind mixes the buoyant warm bubble of air with the surrounding cooler air. The energy dissipates into the next layer; thus, cell size reduces from larger to smaller. The larger cells act as refractive elements, and the smaller cells act as diffractive elements. In general, the smallest and largest cells determine the inner (l_0) and outer (L_0) scales of turbulence [Max, 2010]. The inner scale defines the size of the smallest inhomogeneities in the turbulence, below which we use fluid viscosity to describe flow. The outer scale defines the point beyond which the turbulence becomes anisotropic, resulting in structural and refractive index effects [Tofsted, 2000].

Fried's atmospheric coherence length, r_0, [Fried, 1967] is the standard parameter used to characterize the point spread function (PSF) for imaging through the atmosphere [*seeing* conditions, Martinez, 2010). This can be computed from the path-length integrated c_n^2 as

$$r_0^{-5/3} \equiv \frac{2.91}{6.88}\left(\frac{2\pi}{\lambda}\right)^2 \int_0^L \left(1-\frac{z}{L}\right)^{5/3} c_n^2 dz \equiv \frac{2.91}{6.88}\left(\frac{2\pi}{\lambda}\right)^2 \left(\frac{3}{8}\right)\left\langle c_n^2 L\right\rangle. \quad \textbf{(1)}$$

Here, λ is the monochromatic wavelength, L is the integrated line-of-sight (LoS) path length, and the "constant-equivalent" average index of refraction structure constant $\left\langle c_n^2 L\right\rangle$ is defined as if c_n^2 were constant along the entire path. Note that r_0 is inversely proportional to c_n^2 and thus to the strength of turbulence. Algorithms used to mitigate image degradation and analyze signals increasingly depend on the character and strength of the turbulence.

Figure 1 contains images of a standard target (USAF 1951 resolution test chart) taken during a warm day in California as the sun heated the atmosphere and LoS turbulence increased such that the aperture diameter to the coherence radius D/r_0 increased.

Even though the scene is not monochromatic, it is obvious that perceived image quality correlates with D/r_0. Consequently, D/r_0 can be used as a dimensionless, macroscopic turbulence strength parameter. In practice, we find a D/r_0 of ~20 produces images that have insufficient high spatial frequency detail and cannot be reliably improved by image processing.

Fried postulated that there is some probability of getting a Lucky or clear image through turbulence [Fried, 1978]. Many algorithms rely on this probability to recover high spatial frequency content. Hufnagel determined that if wavefront distortion could be corrected, the probability would increase [Hufnagel, 1989]. Zernike polynomials are used for describing aberrations in optical systems and are often used to describe the wavefront distortion associated with atmospheric turbulence [Noll, 1976; Born, 1965]. The first twelve Zernike degrees of freedom (DOF) are shown on the left in Figure 2. The right image shows the improvement in the probability of getting a Lucky image with different DOFs of Zernike corrections.

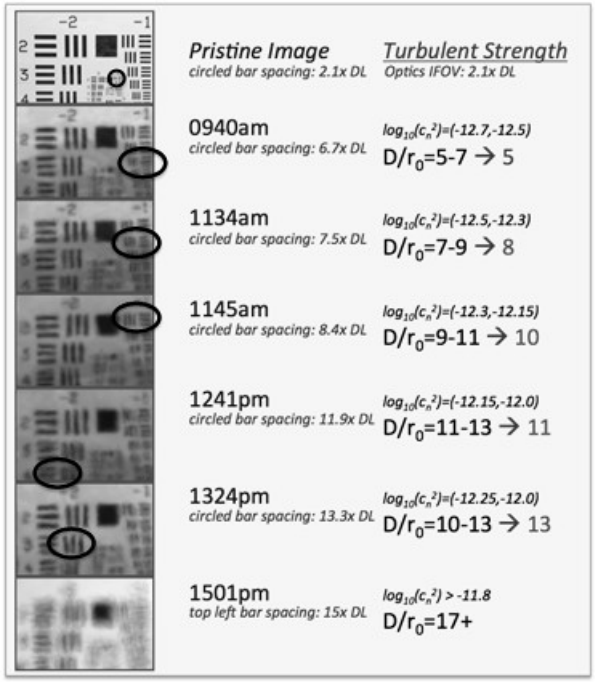

Figure 1. Turbulence strength chart. The target is taken through increasing levels of turbulence characterized by D/r_0 shown on the right. The USAF 1951 resolution test chart aids in extracting an "apparent turbulent resolution" that can be directly compared to a scintillometer measurement.

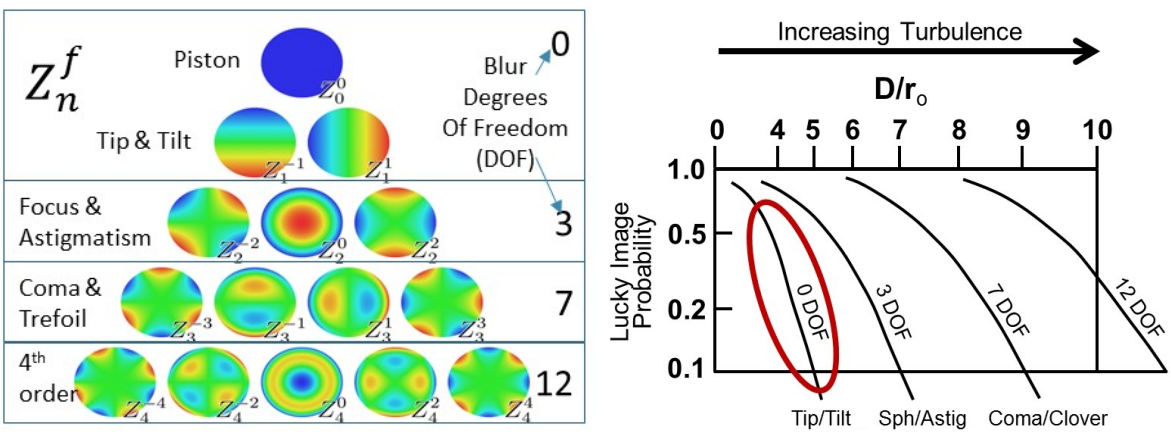

Figure 2. (left) The first twelve Zernike degrees of freedom, and (right) the probability of getting a Lucky image with different DOFs of Zernike corrections

Adaptive optics (AO) systems have been used for years in astronomy to correct for the wavefront distortion associated with atmospheric turbulence [Beckers, 1993]. For scene-based Shack-Hartmann AO systems the source is not completely coherent, so interferometers are not used. Instead, an image of the pupil is projected onto a lenslet array, such that each lenslet represents a different portion of the entrance aperture. Each lenslet images the scene onto a different portion of an image plane. In the absence of turbulence, the images of the point source are uniformly distributed based on the lenslet configuration. With wavefront distortions, the images of the point source will shift from their nominal positions. The corresponding pixel shifts are related to the slopes of the phase of the wavefront for each aperture location. Algorithms for extracting the wavefront distortion exist, but these all rely on high spatial frequency content and typically require a point source in the scene. The phase map derived from these algorithms generates the commands to a deformable

mirror that corrects for the wavefront distortion associated with turbulence. The algorithms for detecting the shifts must be fast enough to change the mirror as the turbulence changes.

While AO works well for astronomical viewing, the same methods do not work well for complex imagery from long-range horizontal paths. Some Shack-Hartmann analysis has been done for astronomical extended sources with this sensor type [Sidick, 2007, 2013; Lukin, 2010, Rais, 2016] but this work has not been extended to horizontal paths. The Army Research Laboratory passive adaptive imaging system is specifically designed to mitigate horizontal path turbulence [Tofsted, 2016], but its implementation includes moving parts not suitable for a compact AO system. Each of these methods for extended sources uses the received imagery to compute pixel shifts associated with wavefront distortion, and all suffer from the same lack of high spatial frequency content characteristic of high turbulence. Currently no adequate compact, real time solution exists for correcting significant long-range horizontal path–induced degradation.

2.0 Project

The goal of this project is to develop a compact AO system for long-range horizontal paths that improves severely degraded images. To do this, we are leveraging the statistical tools developed as part of an earlier NNSS Site Directed Research and development (SDRD) project [O'Neill 2016, Terry 2016] and AO work from literature.

There are two key aspects to this research. First, instead of using a lenslet array, we are leveraging commercial off-the-shelf (COTS) cameras and filters to create a red/green/blue (RGB) wavefront sensor (WFS) [O'Neill 2018]. This allows the same imagery used for obtaining the wavefront distortion to be provided seamlessly to the user while being tolerant to platform motion. It also allows us to access second- and third-order statistics via RGB color separation. We use the method to obtain temporal variance images developed in an FY 2013 SDRD project "Passive Method to Characterize Atmospheric Turbulence" [O'Neill 2014, Terry 2014] to extract high spatial frequency content associated with the scintillation index; this helps determine wavefront distortion, even with limited high spatial frequency content in the scene. By updating this variance image at each frame, new pixel shifts can be obtained on a frame-by-frame basis.

Figure **1**a shows the RGB WFS block diagram and Figure 3b shows the hardware developed in FY 2015 and FY 2016. Solar illumination reflects off the scene and enters the three sub-apertures. When the telescope is focused and no turbulence is present, the three images align perfectly. Because individual light rays go through different points of a plane before or behind focus, any defocus shows up as a pixel shift. When in focus, the pixels are oriented to the same point on the image plane, but when out of focus, the shifted pixels indicate degrees of focus error.

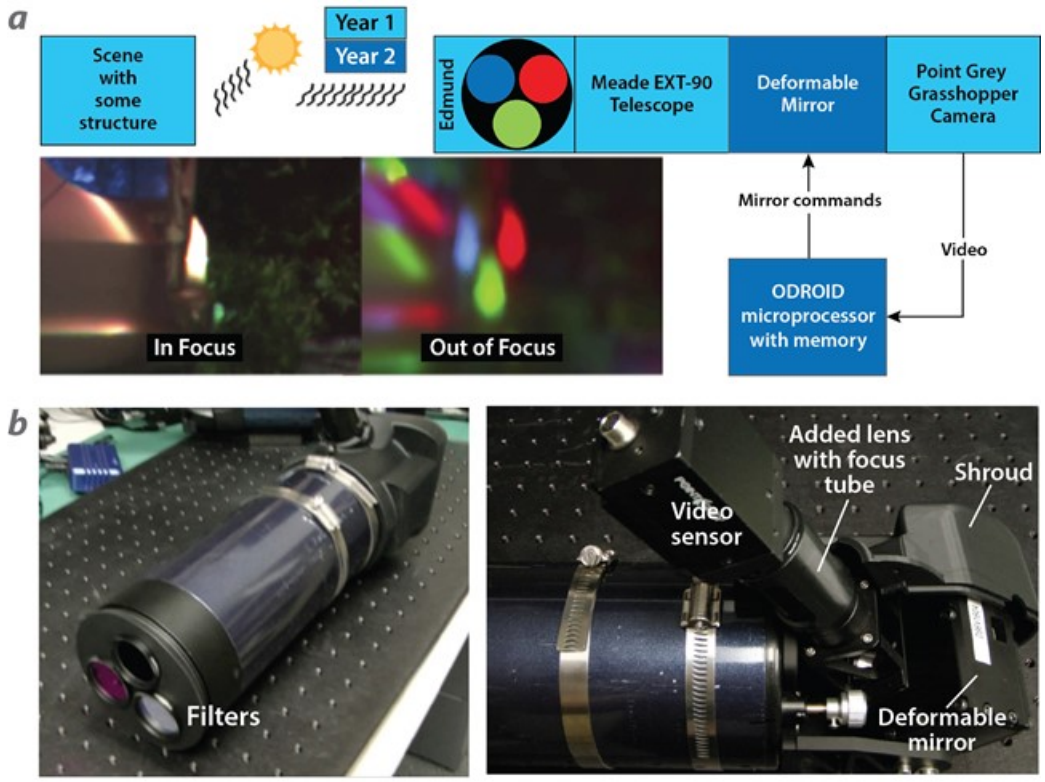

Figure 1. (a) RGB wavefront sensor FY 2015 block diagram and (b) hardware. The sun illuminates the scene with some structure. The reflected light enters the three filters at the entrance to the telescope. When in focus all three images align, but out of focus the pixel shifts correspond to the slope of the phase errors. These errors can be used to compute commands to a DM.

In our previous paper we described the Meade EXT-90 Maksutov-Cassegrain telescope and a Point Grey Grasshopper camera used for our first breadboard. We verified the operation of this camera with a COTS mobile Samsung-based 8-CPU single-board computer (SBC) that drives the USB3 camera, runs Linux, operates on battery, and offers WiFi hot spot connectivity. ODROID SBC uses the same processor as is on a Samsung Galaxy Tablet making porting to a tablet easier in the future. Since that paper, we integrated a DM into our telescope making the RGB wavefront sensor a portable AO system that improves overall image quality and will enable existing algorithms to further that improvement. A new shroud was made using our 3-D printer to enclose the DM. Because we placed the DM at the location of the current mirror, we are not at a pupil and thus not imaging the entrance aperture (i.e., the DM is located at a defocus plane near a pupil). Figure **2** shows the mirror piston positions, mirror, and the mirror installed in the RGB WFS.

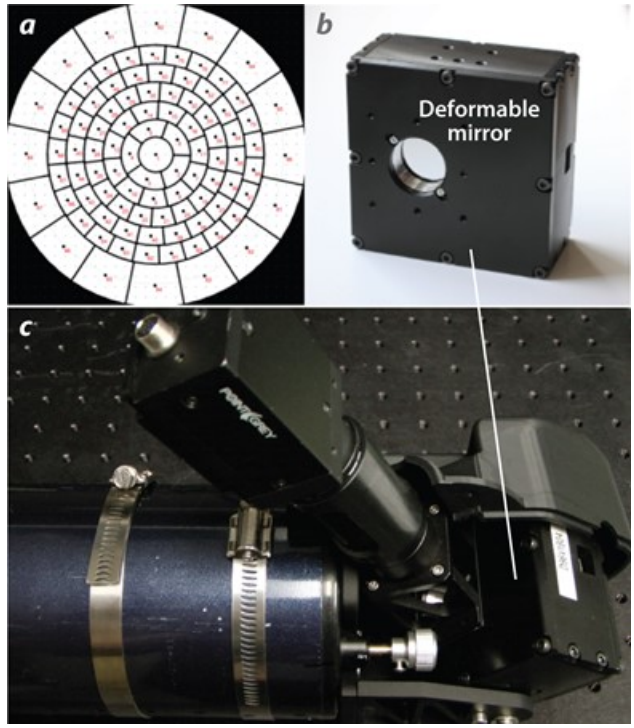

Figure 2. (a) 96 mirror piston positions, (b) mirror, and the (c) mirror installed in the RGB WFS

As can be seen in Figure 1, the filter assembly reduces the apertures and thus increases the *f*/# of the system; in Year 2 we updated our filters to improve both spectral bandwidth and *f*/#. We used the measurement of the relative spectral response of the Point Grey Grasshopper taken in Year 1 [O'Neill 2017] and ran our selection algorithm considering COTS filters.

We developed software to control the DM and compute the variance images. The variance image developed in the earlier SDRD project enhances the turbulent flows even with minimal image contrast and, thus, provides pixel shifts even in extremely high turbulence. While other AO methods rely on the structure in an image, using the variance image relies on the variation over time of the turbulence. Because we have three co-aligned apertures, the pixel shifts in the variance image correspond to the phase shifts associated with the sub-aperture locations. Color cameras automatically demosaic imagery by converting Bayer pixel color planes to RGB so the user sees only a color picture, which typically has mixing of the original color planes. Our processing is done on the raw Bayer pixels; therefore, the color separation remains intact, producing images directly associated with the three apertures.

In our current implementation, we compute pixel shifts via a phase shift in the Fourier domain. Given an intensity measurement at a focal plane at pixel location *x*, *y*, at time *t*, and based on proportionality to Kolmogorov's ansatz [Kolmogorov 1941], we define the received flux variance as the normalized variance over all pixels on the focal plane over *n* samples in Δt increments as

$$\sigma_z^2(x,y,t) = \frac{\langle I(x,y,\tau)^2\rangle_{\tau=t_0 to\ t_0+n\Delta t} - \langle I(x,y,\tau)\rangle^2_{all\ x,y\ \&\tau}}{\langle I(x,y,\tau)\rangle^2_{all\ x,y\ \&\tau}}\,. \qquad \textbf{(2)}$$

In this equation, the variables *x*, *y*, and *t* represent the *x* pixel location on the detector, the *y* pixel location on the detector, and the time of the frame. The variable *I* represents radiant flux at the pixel in counts.

To extract only the turbulence information, and not the scene or sensor noise, for each row, r, or column, c, in the image, the 1-D Fourier transform is computed to obtain the 1-D power spectral density (PSD) of turbulence, $\varphi(k)$. In practice, a fast Fourier transform is used. For horizontal calculations we define k as the spatial frequency in radians/pixel, and the estimated 1-D PSD for each row, r, for the Bayer red (R) channel, is computed as:

$$\phi_R(k_x, y = r, t) = \sum_{x=0}^{N-1} \sigma_{z_R}^2 (x, y = r, t) e^{-ik_x x/N}. \quad \textbf{(3)}$$

This is repeated for green (G) and blue (B). Because we use the relative shifts between colors, any platform motion is cancelled out which is a critical requirement for compact operation. We compute the relative phase shift in the image in radians for red to green as

$$\alpha_{R/G}(k, r, t) = argMax(FT^{-1}[\phi(k_x, y = r, t)\phi_G^*(k_x, y = g, t)]) \ . \quad \textbf{(4)}$$

This process is repeated for G-B and B-R to get all three cases. To get the horizontal pixel shifts, we then multiply by the frequency such that

$$\Delta x(r, t) = \sum_{k_x} \alpha_{R/G}(k_x, r, t)/k_x \ . \quad \textbf{(5)}$$

This process is repeated for all columns to get the vertical shifts.

Because we did not place the mirror exactly at a pupil, but instead at a defocus plane, (i.e., near, but not at, an image plane), we speculated that we could measure the relative pixel shifts for the different actuator positions and determine a matrix solution to control the DM.

Consider a point in the object plane. Because the object is in the far field, rays from this point intersect the entrance aperture with a single angle of incidence. The location of these ray bundles at subsequent positions within the telescope depends on the angle of incidence, such that the location on the entrance aperture is $[x(p_x,p_y),y(p_x,p_y)]$. **Figure 3** shows a cartoon of ray bundles for a given object point, at the entrance aperture, the DM, and the detector (focal plane array, FPA) plane. Note that, in the absence of turbulence (or any defocus), this bundle will focus to a point at the image plane; because the detector has been defocused, however, the bundle has a finite area at the FPA. If the entrance aperture is divided into several sub-apertures, the bundle at the FPA will be separated into the equivalent number of smaller bundles, each with the appearance of the object point, albeit blurred. With focus errors (such as those induced by turbulence), these multiple images shift apart.

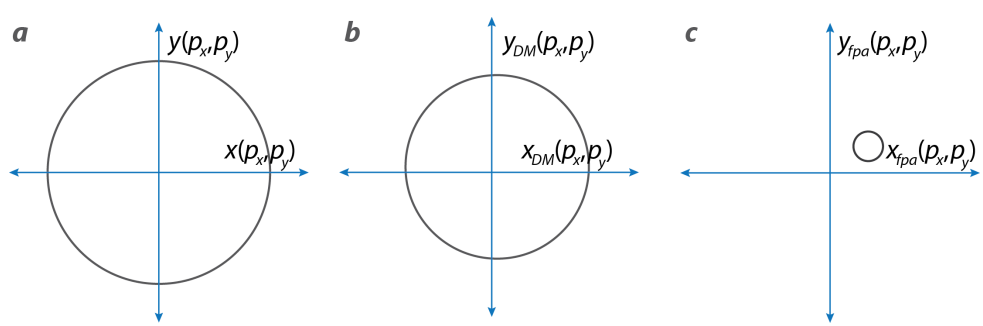

Figure 3. (a) Ray bundle at entrance aperture, (b) ray bundle at DM (note that this is off center as it moves toward (c) ray bundle (PSF) at the FPA

If the DM were at an exit pupil, the bundle in Figure 8b would look the same as those in Figure 8a. This is further illustrated in the extreme case **Figure 4** where we manually took an image of a specular reflection off a car bumper through focus.

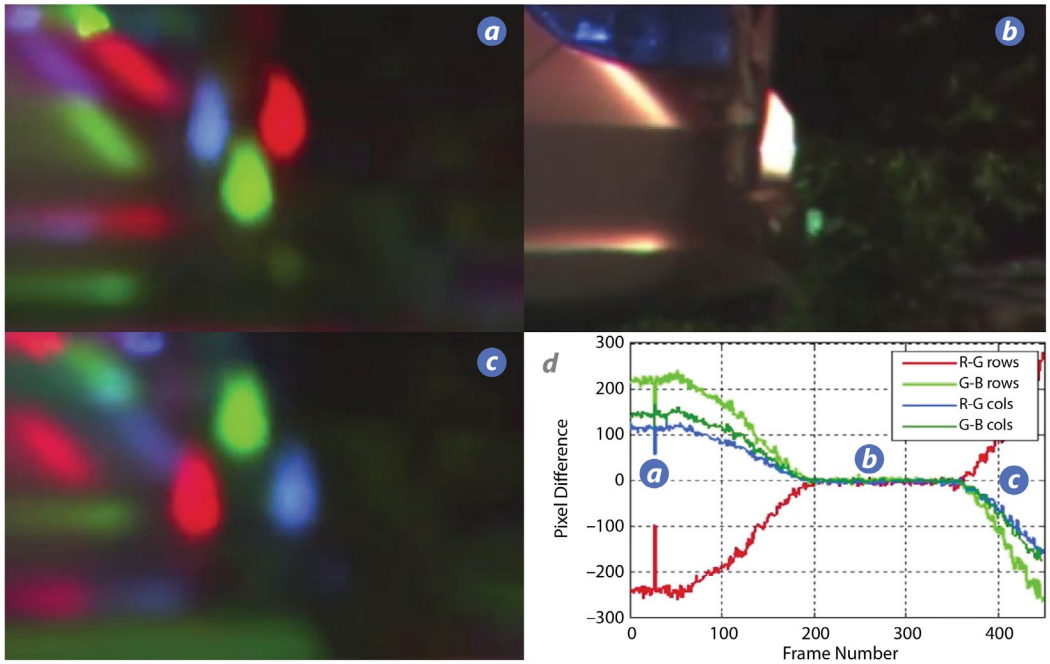

Figure 4. (a) Defocus forward of image plane, (b) at image plane and (c) in aft of image plane. (d) The plot shows pixel shifts as the video went through focus that can be exploited when caused by turbulence.

We developed a method to separate the image into a number of blocks in order to determine the relationship between the relative pixel shifts in these blocks and the required voltages to counter these shifts. Using a number of assumptions, based on the PSFs derived from the wave equation and the literature provided by OKO, we mathematically determined a likely relationship between the measured R-G pixel shifts and DM deformation in *z,*

$$(x_r(b) - x_g(b))k_{x_{fpa}} + (y_r(b) - y_r(b))k_{y_{fpa}} = 2\big(k(g) - k(r)\big)(z(x_{DM}, y_{DM}, V) + c)\ , \qquad \textbf{(6)}$$

where (x_r, y_r) is the pixel location for the red color plane in block b, (x_g, y_g) is the pixel location for the green color plane in block b, k is the wavenumber = $2\pi/\lambda$, z is the mirror deformation at (x_{DM}, y_{DM}) for voltage V, and c is a constant related to the original angle corresponding to the position of the point at the object. This calculation is performed for every block, color plane, and direction. A correction factor is required for each shift to account for the fact that the four color planes (R, G1, G2, B of the Bayer mask) are a pixel apart.

From the OKO literature, z is proportional to V^2 (Vdovin 2013). Because this quadratic is based on an approximation between electrostatic pressure and voltage, we changed the exponent to be a variable, resulting in the matrix equation

$$sign\,(\overrightarrow{\Delta V}) \cdot \left|\overrightarrow{\Delta V}\right|^e = A\overrightarrow{\Delta p}, \qquad \textbf{(7)}$$

where e is the exponent power between 0 and 2, initially set to 1.0, $\overrightarrow{\Delta p}$ is the relative shift as a Mx1 vector where M = (# of dimensions, *xy*)(# of colors, *clr*) (# of blocks, *b*), A is an N×M matrix of coefficients, where N is the number of actuators positions, and $\overrightarrow{\Delta V}$ is an N×1 vector of delta voltages.

Because the pixel shifts have polarity, care is required to determine the actual delta voltages. We began with a linear solution to see if it would converge. We found the relationship between delta shifts and delta

voltage to be crucial; thus, the calculated delta shifts between colors needed to be offset from delta shifts corresponding to the center voltage. The calibration set up uses a grid pattern of distinct spots that match the desired image blocks and is placed at the focus of an optical collimator (lab equipment). The RGB wavefront sensor is placed in front of the collimator to receive the corresponding ray bundle. A block diagram of the test configuration and an example image of the 40 blocks (8x5) collected by the RGB WFS is shown in Figure 5.

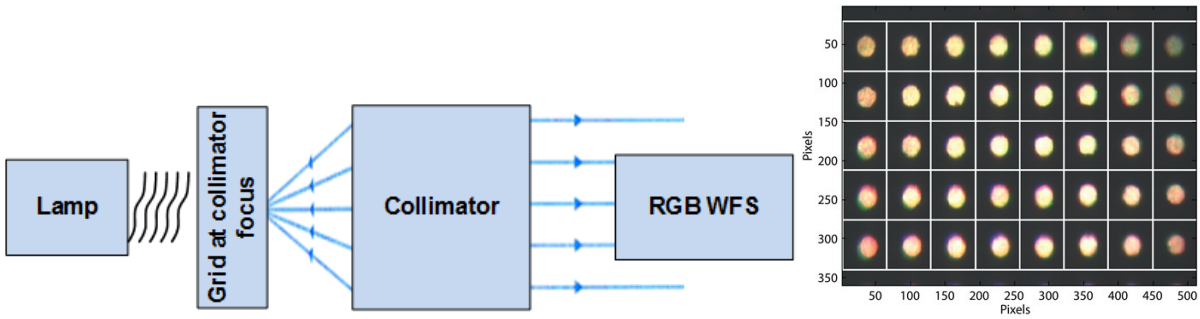

Figure 5. Test configuration and grid pattern used for calibration. We set each block to be 64 × 64 pixels in the raw color planes. Note that using the raw data results in half the number of pixels that result from Bayer interpolation.

The deformable mirror is commanded for each of the 36 unique mirror actuator combinations and corresponding images are saved. These images are analyzed for the relative pixel shifts for each block corresponding to delta voltages to create vector, Δp. From this we then compute the solution for A (the conversion matrix), with $e = 1$ as

$$A = \left(\overrightarrow{\Delta p}\right)^{-1}\left(sign\left(\overrightarrow{\Delta \mathrm{V}}\right) \cdot \left|\overrightarrow{\Delta \mathrm{V}}\right|^{e}\right). \tag{8}$$

Once matrix A was computed, we tested this set of coefficients by slightly defocusing the collimating telescope within the range of motion of the DM. We added a relaxation parameter for our implementation to determine if the solution would converge. For each block, we use our phase correlation registration algorithms (that were implemented on an SBC in FY 2016) on received variance images (or static images on the bench) to extract pixel shifts. The program then computes the estimated voltage error associated with the measured shifts as

$$\widehat{\Delta \mathrm{V}} = \mathrm{rA}\overrightarrow{\Delta p}, \tag{9}$$

where r is a relaxation parameter between 0 and 1. Using this estimate, we compute the new mirror voltage as

$$\mathrm{V(t)} = \mathrm{V(t - \Delta t)} - \left(sign(\widehat{\Delta \mathrm{V}}) \cdot \left|\widehat{\Delta \mathrm{V}}\right|^{e}\right), \tag{10}$$

where e was equal to one for our initial test. Using multiple mirror initialization voltages, we saw this method converge in about eight frames using a relaxation parameter of 0.25, as indicated in Figure 6.

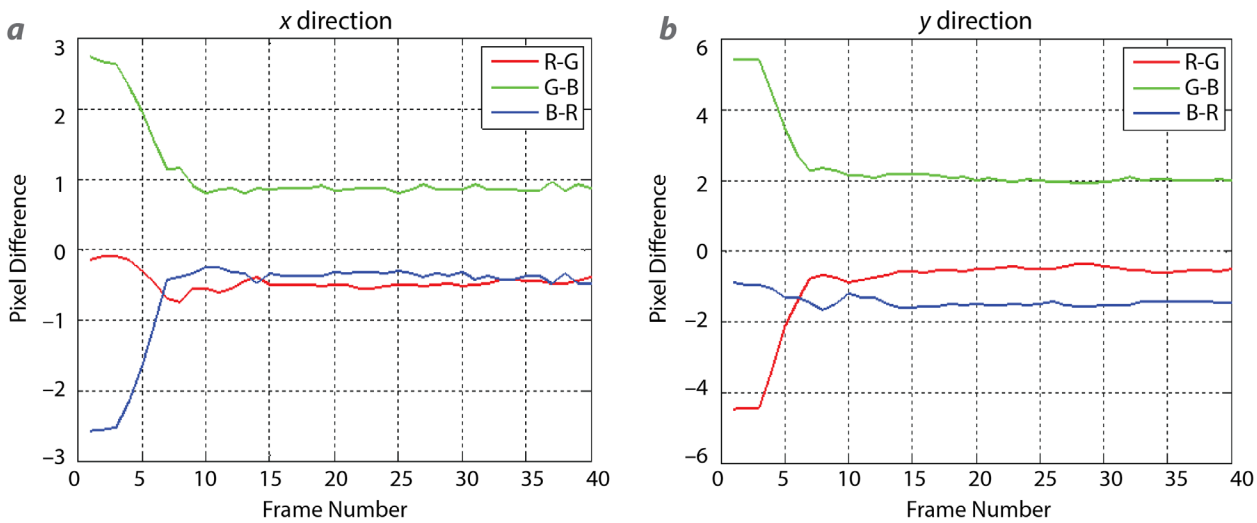

Figure 6. Pixel difference equal to focus error versus frame number for (a) *x* and (b) *y* directions. The solution converges in about eight frames.

The images associated with the starting point, frame 4, and frame 8 for this initial test are shown in Figure 7.

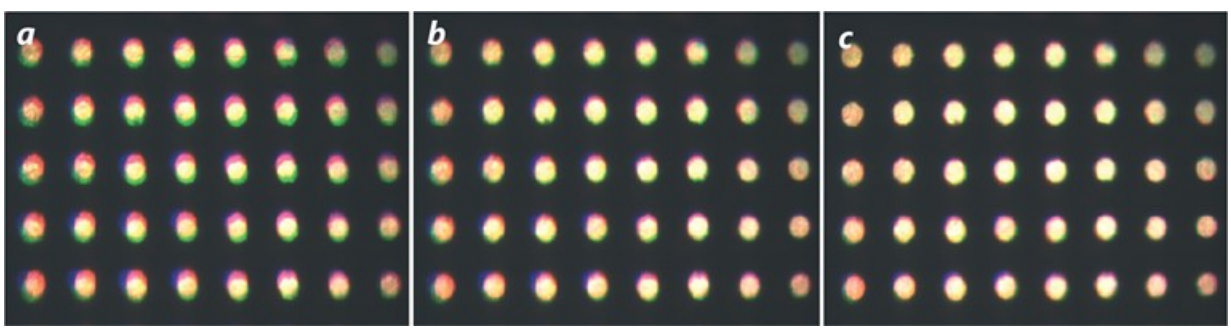

Figure 7. Example mirror control results for bench test case with 0.25 relaxation. (a) No correction (>8 total pixel error), (b) four frames of correction (<4 pixel error), and (c) 8 frames of correction (~2 pixel error).

Figure 7a shows the image at the initialization voltage. Note that all three colors are well separated, indicating defocus. By about the fourth frame, the error is cut in half and by the eighth frame it is within the measurement error of the phase correlation registration algorithms with the exception of the G-B shifts.

On 5 March 2018, we did preliminary roof top tests viewing a street sign from about 700 meters away. These tests were done with only turbulence correction knowing that image stabilization and registration will further improve these results. We visually verified improvement in low, medium and high turbulence conditions. Low turbulence was with cloud cover, low photon count and about 15 mph winds with gusts up to 25 mph. Medium and high turbulence were full sun. Not apparent in still images is the fact that this turbulence correction hardware significantly increases the probability of getting a Lucky image allowing algorithms to be much more effective. Example images for turbulence uncorrected and corrected are provided in Figure 8.

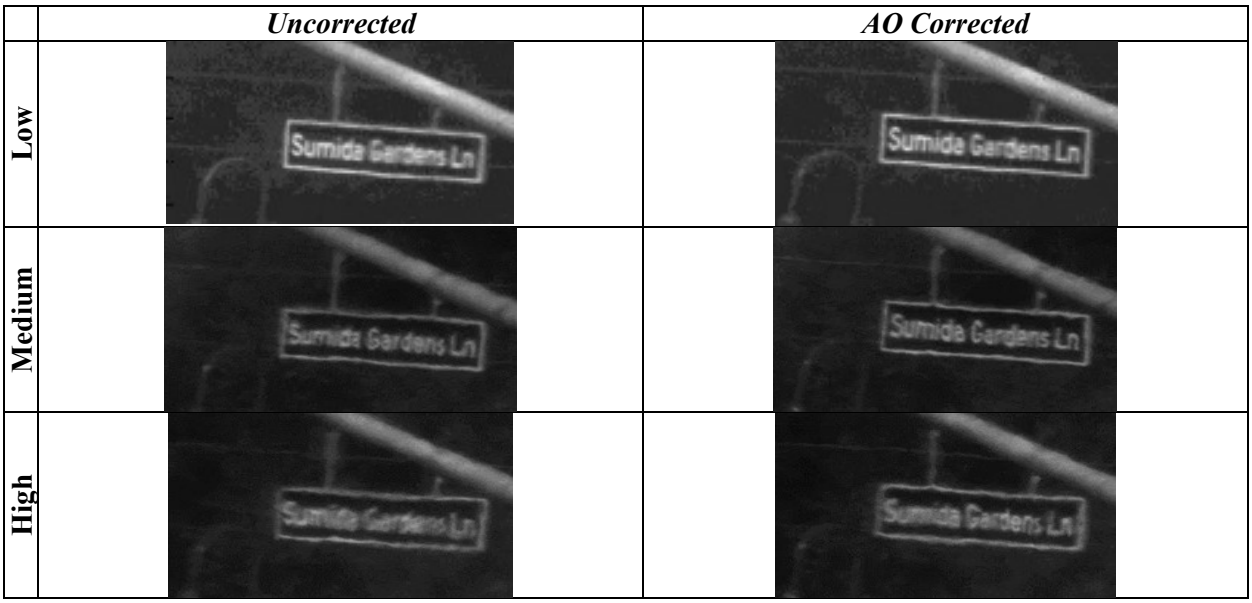

Figure 8. Uncorrected and corrected images for low, medium and high turbulence conditions with no image stabilization or registration. Note that each case shows some improvement. Not apparent in these still images is the increase in the probability of getting a Lucky image with the hardware correction.

Note that the corrected high turbulence image is similar to the uncorrected medium turbulence image. In addition, we presented a live demonstration of this compact, real time turbulence correction technology.

3.0 Summary and Path Forward

We have created a prototype portable AO system using low-cost COTS components. The keys to this work are the three-color aperture configuration and the use of the temporal statistics associated with the variance image to improve the ability to get pixel shifts even in high turbulence. We selected and integrated a DM and a suitable SBC into our system. The Meade telescope fold mirror and shroud were replaced with the DM and a new shroud printed on our 3-D printer. We created a bench setup that allowed us to directly correlate relative pixel shifts between our three colors to mirror commands. We used this same setup to verify our ability to correct for focus errors on the bench. We seamlessly demonstrated this technology to potential sponsors at a range of 700 meters allowing them to see what is possible in a small form factor. We collected preliminary data with visual verification of the ability of our system to improve image quality.

We hope to implement improvements to this prototype in the future including implementation on a tablet, image stabilization, and registration. We would like to more rigorously evaluate the improvement of our system by using a 1951 Air Force target, a scintillometer and our previously developed analysis tools to determine image quality and image quality variance for each test case.

4.0 Acknowledgments

The authors wish to thank Dr. Howard Bender for his support in completing this work and Dr. Rusty Trainham for their help in data collection and sensor characterization. The authors also wish to thank Dr. David Tofsted of Army Research Labs for his insights into AO and turbulence.

This manuscript has been authored by Mission Support and Test Services, LLC, under Contract No. DE-NA0003624 with the U.S. Department of Energy, National Nuclear Security Administration, Office of Defense Programs, and supported by the Site-Directed Research and Development Program. The United States Government retains and the publisher, by accepting the article for publication, acknowledges that the United States Government retains a non-exclusive, paid-up, irrevocable, worldwide license to publish or reproduce the published form of this manuscript, or allow others to do so, for United States Government purposes. The U.S. Department of Energy will provide public access to these results of federally sponsored research in accordance with the DOE Public Access Plan (http://energy.gov/downloads/doe-public-access-plan). The views expressed in the article do not necessarily represent the views of the U.S. Department of Energy or the United States Government. DOE/NV/03624—0361.

5.0 References

Beckers, J. M., "Adaptive optics for astronomy: Principles, performance, and applications," *Ann. Rev. Astron. Astrophys.* **31** (1993) 13–62.

Born, M., E. Wolf, *Principles of Optics*, Section 9.2, Pergamon, New York, 1965.

Fried, D. L., "Optical heterodyne detection of an atmospherically distorted signal wavefront," *Proc. IEEE* **55** (1967) 57–77.

Fried, D. L., "Probability of getting a lucky short-exposure image through turbulence," *J. Opt. Soc. Am.* **68** (1978) 1651–1658.

Hufnagel, R. E., "The probability of a lucky exposure," Tech. Memo, REH-0155, Perkin-Elmer, Norwalk, Connecticut, February 1989.

Kolmogorov, A. N., "The local structure of turbulence in incompressible viscous fluid for very large Reynolds numbers," *Dokl. Akad. Nauk SSSR* **30**, 4 (1941) 301–305.

Lukin V. P., N. N. Botygina, O. N. Emaleev, P. A. Konyaev, "Wavefront sensors for adaptive optical systems," *Meas. Sci. Rev.* **10**, 3 (2010) 102–107.

Martinez, P., J. Kolb, M. Sarazin, A. Tokovinin, "On the difference between seeing and image quality: When the turbulence outer scale enters the game," *European Southern Observatory Messenger* **141** (2010) 5–8.

Max, C., Lecture 3 of Astronomy 289C: Adaptive Optics and its Applications, University of California, Santa Cruz, April 8, 2010.

Noll, R. J., "Zernike polynomials and atmospheric turbulence," *J. Opt. Soc. Am.* **66** (1976) 207–211.

O'Neill, M. D., D. Terry, A. Potter, I. McKenna, "Passive method to characterize atmospheric turbulence," in *Site-Directed Research and Development*, FY 2013, National Security Technologies, LLC, Las Vegas, Nevada, 2014, 125–135.

O'Neill, M. D., D. Terry, "Portable COTS RGB Wavefront Sensor," *MSS Passive Sensors*, Gaithersburg, Maryland, 2016.

O'Neill, M. D., D. Terry, "RGB wavefront sensor for turbulence mitigation," in *Site-Directed Research and Development*, FY 2016, National Security Technologies, LLC, Las Vegas, Nevada, 2017, 109–117.

O'Neill, M. D., D. Terry, "RGB wavefront sensor for turbulence mitigation," Patent Application 16231023, Filed 21 December 2018.

Rais, M., J.-M. Morel, C. Thiebaut, J.-M. Delvit, G. Facciolo, "Improving the accuracy of a Shack-Hartmann wavefront sensor on extended scenes," *6th International Workshop on New Computational Methods for Inverse Problems (NCMIP)*, May 2016, Cachan, France, https://hal-enpc.archives-ouvertes.fr/hal-01344949/document, accessed Ocotober 5, 2016.

Sidick E., J. J. Green, C. M. Ohara, D. C. Redding, "An adaptive cross-correlation algorithm for extended scene Shack-Hartmann wavefront sensing," in *Adaptive Optics: Analysis and Methods/Computational Optical Sensing and Imaging/Information Photonics/Signal Recovery and Synthesis Topical Meetings on CD-ROM*, OSA Technical Digest (CD) (Optical Society of America, 2007), paper JTuA7, http://www.meripet.com/Papers/JTuA7.pdf, accessed October 5, 2016.

Sidick, Erkin, "Extended scene Shack–Hartmann wavefront sensor algorithm: Minimization of scene content dependent shift estimation errors," *Appl. Opt.* **52** (2013) 6487–6496.

Terry, D., M. D. O'Neill, "Passive method to characterize atmospheric turbulence," *MSS Passive Sensors*, Gaithersburg, Maryland, 2014.

Tofsted, D. H., "Turbulence simulation: Outer scale effects on the refractive index spectrum," Army Research Laboratory Technical Report ARL-TR-548, November 2000, http://www.dtic.mil/dtic/tr/fulltext/u2/a384900.pdf, accessed April 6, 15.

Tofsted, D., "Passive adaptive imaging through turbulence," *Proc. SPIE* **9833** (2016) 98330B.

Vdovin, G., O. Soloviev, M. Loktev, V. Patlan, "OKO Guide to Adaptive Optics," Fourth Edition, OKO Technologies, May 2013.